Materials Today Advances 27 (2025) 100603

Contents lists available at ScienceDirect

Materials Today Advances

journal homepage: www.journals.elsevier.com/materials-today-advances/

Computational discovery of Mg-based garnet structures with enhanced battery performance

Sanghyun Kim, Joo-Hyoung Lee *

Department of Materials Science and Engineering, Gwangju Institute of Science and Technology (GIST), Buk-gu, Gwangju, 61005, South Korea

ARTICLE INFO

Keywords:
Multivalent cathode active material
Mg-ion battery
Density functional theory
High performance electrode

ABSTRACT

In the burgeoning landscape of power source technologies, Mg-ion batteries have emerged as a promising alternative to the widely used Li-ion batteries due to the large natural abundance and divalence of magnesium. As an attempt to develop working Mg-ion batteries, for which securing efficient cathode materials with high energy density and ion mobility is crucial, we carry out electronic structure calculations based on density functional theory (DFT) to uncover high-performance garnet-type cathode materials, $Mg_3V_{1.5}Cr_{3.5}O_{12}$ (MVCO) and $Mg_3V_3Mn_2O_{12}$ (MVMO), for efficient Mg-ion batteries. Our DFT calculations demonstrate that MVCO (MVMO) not only achieves a high average voltage of 2.79V (2.69V) and energy density of 856 Wh/kg (821 Wh/kg) but also presents small volume change of 4.5 % (4 %) and low ion migration barrier of 395 meV (190 meV). It is further found out that although oxygen atoms participate in the redox reaction during the (de)intercalation process, the strong orbital hybridization between oxygen and transition metal elements prevents forming $(O\text{-}O)^{n-}$ dimers and thus oxygen release is likely to be suppressed, ensuring structural stability. Combined with high likelihood of successful synthesizability as is evidenced through comparison with the amorphous limits, these materials properties make the proposed garnet-structured magnesium compounds appealing candidates for post-Li energy storage solutions.

1. Introduction

In the pursuit of sustainable energy solutions, the development of advanced battery technologies holds great promise. In this respect, Li-ion batteries have maintained a significant presence in the field of energy storage owing to their superior attributes, including high energy densities, efficient Coulombic performance, minimal self-discharge rates and the ability to utilize various electrodes for a broad spectrum of chemical potentials [1–3]. Over the years, there have been numerous attempts towards the development of next-generation Li-ion batteries with high charge capacities and power densities, aimed towards applications in, for instance, electric vehicles and aerospace applications [4–6] since conventional Li-ion batteries (e.g., $LiCoO_2$, $LiFePO_4$, and $LiMn_2O_4$) do not provide sufficient charge capacities and energy densities for certain applications such as stationary energy storage [7,8]. Alongside these efforts, search for the post-Li battery materials has intensified due to concerns regarding the issues of lithium scarcity arising from rapidly increasing demand and lack of lithium in nature. In this respect, magnesium-ion batteries present a promising alternative that addresses many of the challenges associated with Li-ion batteries. Moreover, magnesium, highly stable, abundant in nature (approximately 10^4 times more than lithium) and widely distributed geographically, offers a compelling solution to resource scarcity concerns [9,10].

In light of increasing concerns over lithium scarcity and the rapidly growing demand for lithium-based resources, research into post-Li battery technologies has expanded significantly. Prominent alternatives under active investigation include alkali-metal-ion batteries, such as sodium- and potassium-ion systems, as well as multivalent-ion batteries based on magnesium, calcium, or aluminum [11,12]. These emerging chemistries offer promising pathways to overcome resource constraints while maintaining high electrochemical performance. One of the most promising attributes of magnesium is its divalent nature which produces a Mg^{2+} ion during the oxidation processes. This divalency of magnesium contributes to a high specific capacity and volumetric energy density. Particularly, the theoretical volumetric capacity of a Mg-ion battery is 3833 mAh/mL, nearly double that of Li ion battery (2046 mAh/mL) [9]. Furthermore, Mg-ion batteries hold a potential to overcome safety risks associated with lithium-based chemistries. The

* Corresponding author.
E-mail address: jhyoung@gist.ac.kr (J.-H. Lee).

https://doi.org/10.1016/j.mtadv.2025.100603
Received 16 February 2025; Received in revised form 3 August 2025; Accepted 4 August 2025
Available online 11 August 2025

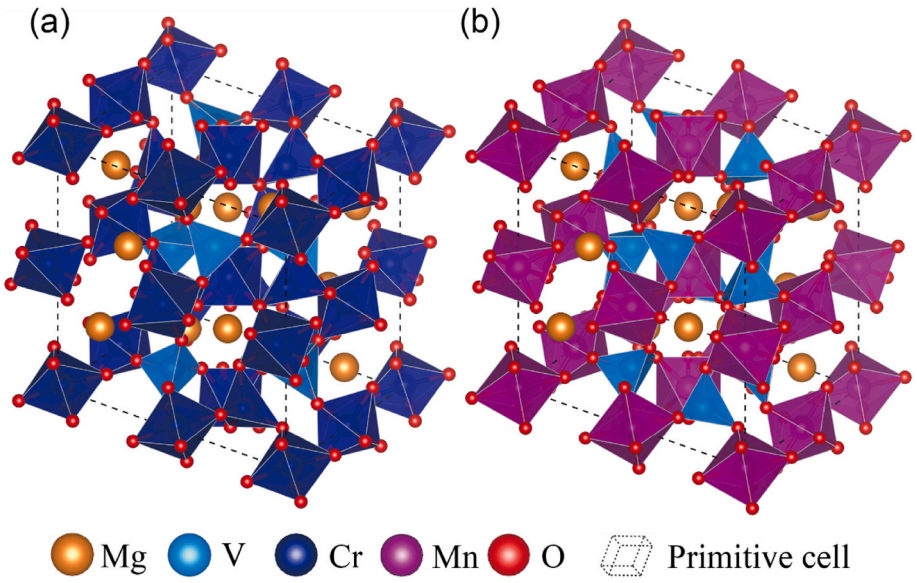

Fig. 1. Crystal structures of (a) $Mg_3V_{1.5}Cr_{3.5}O_{12}$ and (b) $Mg_3V_3Mn_2O_{12}$. The dashed lines denote the boundaries of the primitive cell.

tendency of forming lithium dendrites, which can lead to short circuits and thermal runaway, has been a persistent challenge in Li-ion battery technology [13,14]. In contrast, magnesium deposition and dissolution are expected to occur more homogeneously, reducing the likelihood of dendrite formation and enhancing battery safety [15–17]. As such, Mg-ion batteries present a potential for significantly longer lifespan compared to Li-ion batteries and can achieve faster charging time since Li-ion batteries must limit their charging rates to avoid dendrite formation.

Despite the compelling advantages, the widespread adoption of Mg-ion batteries faces several technical difficulties, particularly in the design of high-performance cathode materials. Firstly, although a high average voltage is necessary for industrial use, most Mg-ion cathode active materials currently operate within a low voltage range, leading to a reduced energy density. In $TMXO_4$ (TM = Mn, Fe, Co, Ni and X = P, Si), the magnesiation voltages are 0.7–0.9V lower than lithiation voltages [18], and the average discharge voltage with TiS_2 nanotubes is 0.98V, compared to 2.1V for lithiation in the same host material [19]. Secondly, the pronounced Coulombic effect of the Mg cation within the cathode materials induces a considerable energy barrier during the intercalation and deintercalation processes, resulting in diminished reversible capacity. For instance, in spinel Mn_2O_4, the migration energy barrier for Mg^{2+} is 600–800 meV, whereas for Li^+ it ranges from 400 to 600 meV [20]. And, the migration energy barrier for Mg^{2+} on a V_2N monolayer is more than double that for Li^+, with values of 0.058eV and 0.025eV, respectively [21]. The limited mobility of Mg^{2+} ions is attributed to both the strong ionic interactions and redistribution of divalently charged cations within the host materials [22].

In this work, we address these important issues by performing first-principles studies, aiming to discover and investigate of novel cathode materials with high energy density for Mg-ion batteries. In addition to complying with industrial goals, ideal cathode active materials must possess high ion mobility, high average voltage and small volume change for structural stability. Here, we propose novel garnet-structured materials, $Mg_3V_3Mn_2O_{12}$ and $Mg_3V_{1.5}Cr_{3.5}O_{12}$, as high-performance Mg-ion intercalation cathode active materials. Through first-principles density functional theory (DFT) calculations, it is shown that these materials exhibit high average voltages, high energy densities and low volume changes. Besides, the energy barrier for Mg-ion migration is sufficiently low that the high ion mobilities can be supported with the host materials to satisfy the requirements for rechargeable battery cathodes.

2. Methods

2.1. Crystal structures

To identify cathode materials, we carry out a combined accelerated screening over the Materials Project database with a machine learning model [23,24] and elemental substitution, which enables the discovery of novel Mg-ion cathode materials, $Mg_3V_{1.5}Cr_{3.5}O_{12}$ and $Mg_3V_3Mn_2O_{12}$. Fig. 1(a) and (b) illustrate the structures of $Mg_3V_{1.5}Cr_{3.5}O_{12}$ and $Mg_3V_3Mn_2O_{12}$, which are in garnet-type structures [25,26] with an $I4\,\overline{3}\,d$ space group and lattice constants of 10.55 Å and 10.6 Å, respectively. In the primitive cell of $Mg_3V_{1.5}Cr_{3.5}O_{12}$, there are six VO_4 tetrahedra, six CrO_4 tetrahedra and eight CrO_6 octahedra. Each VO_4 and CrO_4 tetrahedron is connected with CrO_6 octahedra through a shared oxygen atom. The primitive cell of $Mg_3V_3Mn_2O_{12}$ contains twelve VO_4 tetrahedra and eight MnO_6 octahedra. As in $Mg_3V_{1.5}Cr_{3.5}O_{12}$, each VO_4 tetrahedron is linked with CrO_6 octahedra by a shared oxygen atom. In both structures, a dodecahedron is formed with the Mg-ion occupying its center.

2.2. Computational details

All DFT calculations are conducted with Vienna Ab initio Simulation Package (VASP) [27] by employing the projector augmented wave (PAW) method [28] and Perdew-Burke-Ernzerhof (PBE) parametrization for generalized gradient approximation (GGA) to exchange-correlation functionals [29]. The energy cutoff for the Kohn-Sham wavefunction is set to be 520eV and Brillouin zone integration is carried out over 2 × 2 × 2 k-point mesh [30] using Gaussian smearing methods with 0.05eV as a smearing parameter. It is noted that both the atomic positions and unit cell shapes are optimized. To accurately describe the localized nature of d-electrons in transition metal (TM) species, the GGA + U method, which incorporates a Hubbard-type potential (U) for the d-part of the Hamiltonian, is used with U set at 3.25eV for vanadium, 3.7eV for chromium and 3.9eV for manganese, respectively [31–33]. It is noted that while several studies have included van der Waals interactions and zero-point energy corrections to enhance computational accuracy [34], such effects are expected to be negligible for the MVMO and MVCO structures since these materials are transition metal oxides and do not exhibit layered characteristics. To investigate ion migration, the climbing-image nudged elastic band (CI-NEB) method [35] is applied with five intermediate images, the crystal orbital overlap

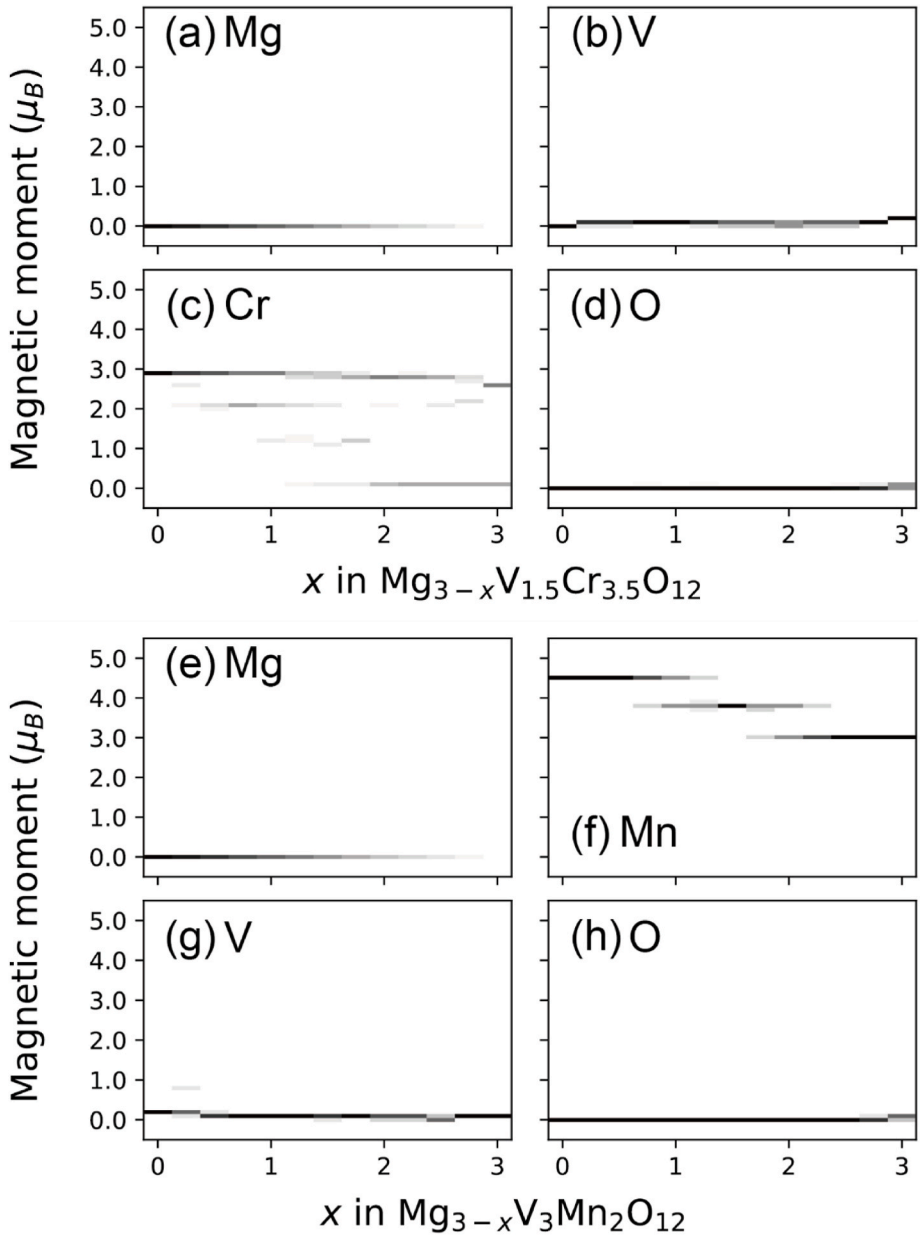

Fig. 2. The magnetic moment distribution in (a–d) $Mg_{3-x}V_{1.5}Cr_{3.5}O_{12}$ and (e–h) $Mg_{3-x}V_3Mn_2O_{12}$ ($0 \leq x \leq 3$) as a function of Mg concentration. For each Mg concentration, the heatmap of magnetic moment with atomic fraction ranging from zero (white) to one (black) is shown with different atomic species: (a, e) Mg, (b, g) V, (c) Cr, (f) Mn, (d, h) O.

population (COOP) is analyzed with LOBSTER [36] to examine the bonding nature between TM elements and oxygen atom in host materials. The COOP values reveal the character of the interatomic bond, that is, the positive (negative) COOP represents (anti-)bonding sates, and zero COOP describes nonbonding states, respectively. The COOP analysis provides an insight into the material's resistance to oxygen release which would lead to irreversible structural distortion.

To investigate synthesizability of the proposed structures, the amorphous limit as suggested by Aykol et al. [37] is calculated. To this end, *ab initio* molecular dynamics (AIMD) are conducted for the supercells of $Mg_{24}V_{12}Cr_{28}O_{96}$, $V_{12}Cr_{28}O_{96}$, $Mg_{24}V_{24}Mn_{16}O_{96}$ and $V_{24}Mn_{16}O_{96}$ with volume 20 % larger than the ground-state crystals. These supercells are subjected to melting at 5000 K for 5000 equilibrium steps and 5000 production steps within an NVT ensemble with a 2 fs time step. To create amorphous structures, forty different snapshots are randomly selected from the production stage, which are then rapidly quenched to 0 K by performing conjugate gradient optimization on all geometric degrees of freedom. This process relaxes the configurations to the local minima of the corresponding basins in the potential energy landscape and determines the energies of the representative amorphous configurations. For statistical analysis, N configurations (N = 2, 4, 8, 16) are randomly selected from 40 quenched configurations, and the corresponding probability density functions (PDFs) representing the amorphous limit are generated from the amorphous energies, assuming the Gaussian distributions with standard deviation of 0.012eV/atom that is the maximum permissible levels of error for DFT calculations [37].

3. Results and discussion

3.1. Redox reactions in cathodes

To determine the elements participating in the redox process throughout the (de)intercalation processes, the magnetic moments for each atomic species are calculated since the variation in the magnetic

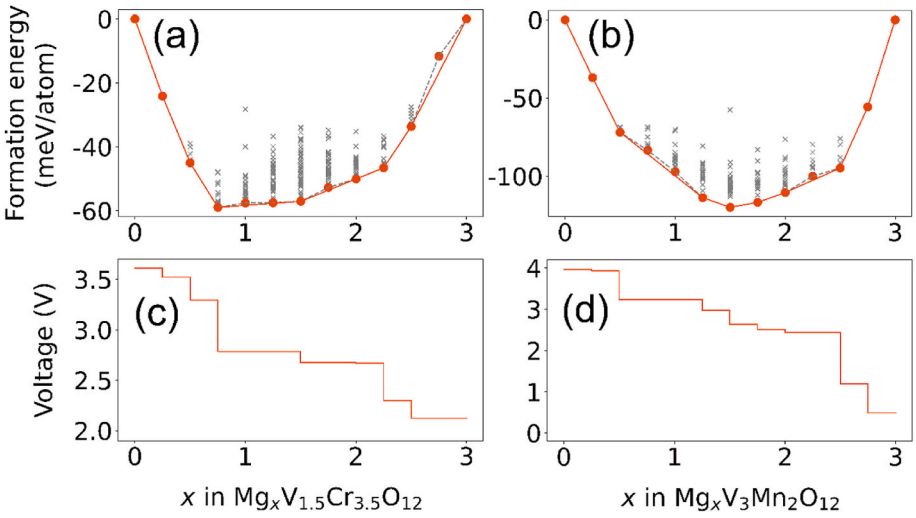

Fig. 3. Formation energy convex hull construction (a, b) and corresponding voltage profile (c, d) for $Mg_xV_{1.5}Cr_{3.5}O_{12}$ and $Mg_xV_3Mn_2O_{12}$. The formation energies of all symmetrically distinct phases are indicated by gray crosses, and stable phases for each Mg-ion concentration are highlighted with solid circles. Energetically stable phases for each Mg-ion concentration are connected by gray dashed lines and intermediate metastable phases are connected by orange lines.

moments provides insights into the oxidation states and electronic configurations of the atomic species, enabling identification of the primary participants in the redox reactions. As is shown in Fig. 2, the average magnetic moments of chromium in $Mg_3V_{1.5}Cr_{3.5}O_{12}$ decrease from 2.93μ_B to 2.65μ_B for CrO_6 octahedra and from 2.97μ_B to 0.16μ_B for CrO_4 tetrahedra, respectively, during the deintercalation process. Similarly, the average magnetic moments of manganese in $Mg_3V_3Mn_2O_{12}$ decrease from 4.54μ_B to 3.06μ_B. In contrast, the remaining atomic species in both compounds show nearly unchanged magnetic moments. This indicates that charge compensation occurs primarily through chromium at $Mg_3V_{1.5}Cr_{3.5}O_{12}$ and manganese at $Mg_3V_3Mn_2O_{12}$, respectively, during Mg-ion (de)intercalation process, thus playing the role of the redox centers.

3.2. Convex hull and voltage profile

In order to analyze the relative thermodynamic stability of partially Mg-ion removed phases during th(de)intercalation process, we calculate the formation energy convex hulls, which are also utilized to evaluate the voltage profiles associated with the electrochemical insertion or extraction of cations. To this end, symmetrically distinct structures containing partially removed Mg-ions are generated using Pymatgen package [38], which is followed by calculating the formation energy of each distinct structure with respect to Mg-ion concentration. The convex hull of the formation energy curve is then constructed through connecting all the ground state energies along the (de)intercalation path as is illustrated in Fig. 3(a) and (b). The negative formation energies of $Mg_3V_{1.5}Cr_{3.5}O_{12}$ and $Mg_3V_3Mn_2O_{12}$ suggest that the corresponding structures are thermodynamically stable during magnesiation, whereas the positive formation energy rule out the presence of $Mg_{2.75}V_{1.5}Cr_{3.5}O_{12}$. According to the convex hull formation energies, six stable structures for $Mg_3V_{1.5}Cr_{3.5}O_{12}$ and seven stable structures for $Mg_3V_3Mn_2O_{12}$ are identified, which suggests that insertion of magnesium of $Mg_3V_{1.5}Cr_{3.5}O_{12}$ ($Mg_3V_3Mn_2O_{12}$) takes place in seven (eight) steps. In both Fig. 3(a) and (b), there is a convex curve, indicating that different phases may coexist [39]. Addressing the phase coexistence and configurational disorder is an important direction for future work.

The voltage (vs Mg/Mg^{2+}) between two different Mg-ion fractions is calculated with

$$V_{x_1,x_2} = \frac{E^{DFT}_{x_1} - E^{DFT}_{x_2} - (x_1 - x_2)E^{DFT}_r}{2(x_1 - x_2)F}.$$

Here, $E^{DFT}_{x_i}$ $(i = 1,2)$ represent the total energy of the proposed materials with x_i cation concentrations, E^{DFT}_r is the ground-state energy of the metallic Mg, and F denotes the Faraday constant, respectively. The factor 2 in the denominator accounts for the number of electrons carried by cation Mg^{2+} [40].

Fig. 3(c) and (d) illustrate the discharge voltage profiles for the stable phases along the (de)intercalation path for the $Mg_3V_{1.5}Cr_{3.5}O_{12}$ and $Mg_3V_3Mn_2O_{12}$, respectively. For $Mg_3V_{1.5}Cr_{3.5}O_{12}$, the voltage ranges between 2.25 and 3.55 V with an average value of 2.79 V vs Mg/Mg^{2+} over the full intercalation path. For $Mg_3V_3Mn_2O_{12}$, on the other hand, the voltage ranges between 0.53 and 3.97 V with 2.69 V as an average. These voltages result in gravimetric and volumetric energy densities of 856 Wh/kg and 3300 Wh/L for $Mg_3V_{1.5}Cr_{3.5}O_{12}$, and 820 Wh/kg and 3133 Wh/L for $Mg_3V_3Mn_2O_{12}$, respectively. Significantly, the average voltages of the proposed cathode active materials are more than twice those of previously studied Mg-ion battery materials, and, moreover, surpass the industrial goal for energy density by more than a factor of two.

3.3. Anion redox chemistry

Fig. 4 illustrates the projected density of states (PDOS) for 3d electrons of TM atoms and 2p electrons of oxygen atoms in $Mg_xV_{1.5}Cr_{3.5}O_{12}$ and $Mg_xV_3Mn_2O_{12}$ $(0 \leq x \leq 3)$. As is illustrated by the PDOS of O-2p, the removal of an electron from the O-2p states during the full demagnesiation process suggests that the oxygen atoms are likely to act as a redox-active site. For such anionic redox reactions (ARRs), the irreversible oxygen release is frequently observed, which can lead to significant degradation of the structural integrity of the cathode active materials, thus reducing their lifespan and overall performance [41].

However, as is shown in Fig. 4, the PDOS of TM-3d orbitals in $V_{1.5}Cr_{3.5}O_{12}$ and $V_3Mn_2O_{12}$ predominantly make orbital overlap with the PDOS of O-2p orbital near the Fermi level, indicating strong orbital hybridization between TM-3d and O-2p orbitals. Additionally, the Bader charge analysis in Fig. 5 demonstrates that the charge density around chromium and manganese (oxygen) atoms gradually increases (decreases) as Mg-ion is deintercalated. This synchronous variation in the charge density highlights the strong electronic coupling between the chromium/manganese and oxygen atoms. This is similar to the cases of Li-ion cathode materials, for example, in ordered $Li_{1-y}Nb_{1/3}Ni_{2/3}O_2$, the averaged Bader charge for Ni (O) progressively increases (decreases) as a result of strong hybridization between Ni-3d and O-2p orbitals and

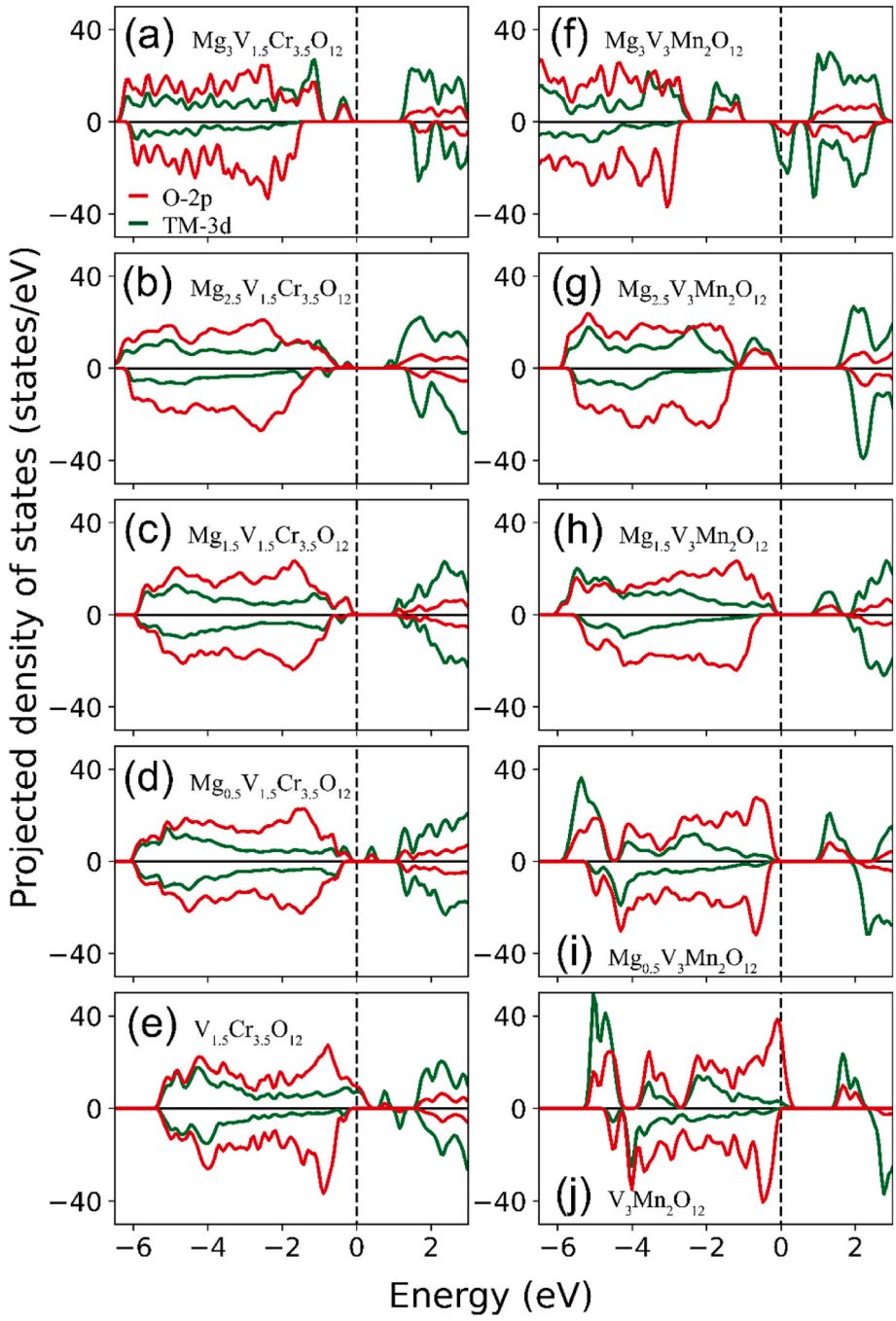

Fig. 4. (a–e) PDOS for (a–e) $Mg_xV_{1.5}Cr_{3.5}O_{12}$ and (f–j) $Mg_xV_3Mn_2O_{12}$ with x varing from 3 to 0. The TMs, including V, Cr, Mn, 3d orbital states are shown in green and oxygen 2p orbital states are colored in red.

enhanced covalency of Ni-O bonds [42]. Furthermore, charge density maps were analyzed to provide an intuitive visualization of charge distribution, as shown in Fig. S1. The results reveal a pronounced covalent bonding between oxygen atoms and transition metal species, which contributed to the structural stabilization of both MVMO and MVCO.

It should be noted that the strong hybridization between the O-2p and TM-3d orbitals stabilizes the oxygen species, preventing forming O_2 molecules and thereby mitigating oxygen gas release despite the ARR activity during the intercalation processes. For example, in layered oxide cathodes, orbital hybridization between TM-d and oxygen 2p orbitals leads to the formation of (TM-O) bonding and (TM-O)* antibonding states. The bonding states, which are below the Fermi level, are crucial for maintaining the crystal structure and indicate a strong covalent interaction between TM and O, forming stable oxygen dimers and preventing O_2 release [43–45]. Also, the ordered Na_2RuO_3 has been reported to suppress oxygen gas release due to significant orbital overlap between Ru-4d and O-2p orbitals [46]. Consequently, the strong orbital hybridization in $Mg_3V_{1.5}Cr_{3.5}O_{12}$ and $Mg_3V_3Mn_2O_{12}$ is highly likely to preserve the structural integrity and longevity despite the involvement of oxygen atoms in the redox process.

To obtain an insight into the bonding nature, the COOPs between chromium and oxygen, between manganese and oxygen, and between oxygen atoms are calculated and presented in Fig. 6 for the Cr-O bonds and O-O bonds in $V_{1.5}Cr_{3.5}O_{12}$ (Fig. 6(a) and (b)) and for the Mn-O bonds and O-O bonds in $V_3Mn_2O_{12}$ (Fig. 6(c) and (d)), respectively, within the

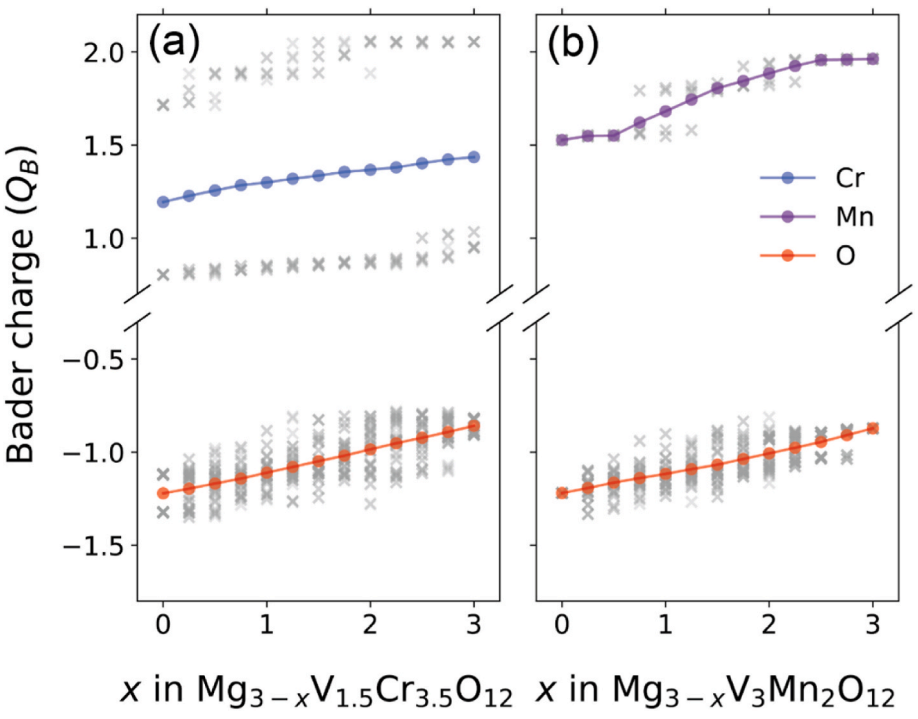

Fig. 5. Bader charge analysis for Cr and O ions in (a) $Mg_{3-x}V_{1.5}Cr_{3.5}O_{12}$, and Mn and O ions in (b) $Mg_{3-x}V_3Mn_2O_{12}$ as a function of x ($0 \leq x \leq 3$). Gray cross symbols denote Bader charges for individual ions while averaged Bader charges are shown as circles with color-coded lines with blue (Cr), purple (Mn), and red (O).

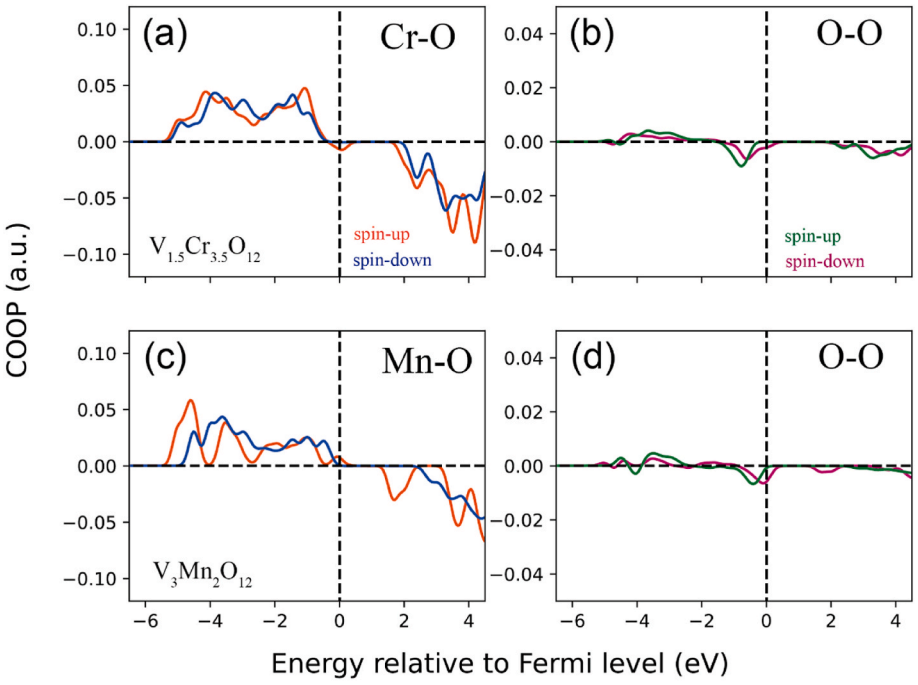

Fig. 6. The COOP of (a) Cr-O and (b) O-O bonds in $V_{1.5}Cr_{3.5}O_{12}$, and (c) Mn-O and (d) O-O bonds in $V_3Mn_2O_{12}$. Cr-O bond and Mn-O bond are depicted with green lines for spin up states and blue lines for spin down states. O-O bonds are represented by yellow lines for spin up states and red lines for spin down states. The vertical dashed line in each plot denotes the Fermi level.

anionic redox regime. For $V_{1.5}Cr_{3.5}O_{12}$, the Cr-O bonds (Fig. 6(a)) shows that positive COOP (bonding states) predominates across nearly the entire energy range below the Fermi level for both spin-up and -down electrons whereas slight negative COOP (antibonding states) appears for spin-up electrons within 0.4 eV from the Fermi level. In contrast, the O-O bonds shows that negative COOP prevails for both spins (Fig. 6(b)). Similarly, while the COOP reveals positive values regardless of spins in the Mn-O bonds of $V_3Mn_2O_{12}$, as illustrated in Fig. 6(c), the O-O bonds mostly show negative COOP, especially near the Fermi level. It is thus understood that electrons are withdrawn from the antibonding O-O states during the ARR process. However, the bonding states between the Cr-3d, Mn-3d and O-2p orbitals are nearly unchanged, which prevents forming $(O\text{-}O)^{n-}$ dimers, implying that oxygen release is highly unexpected.

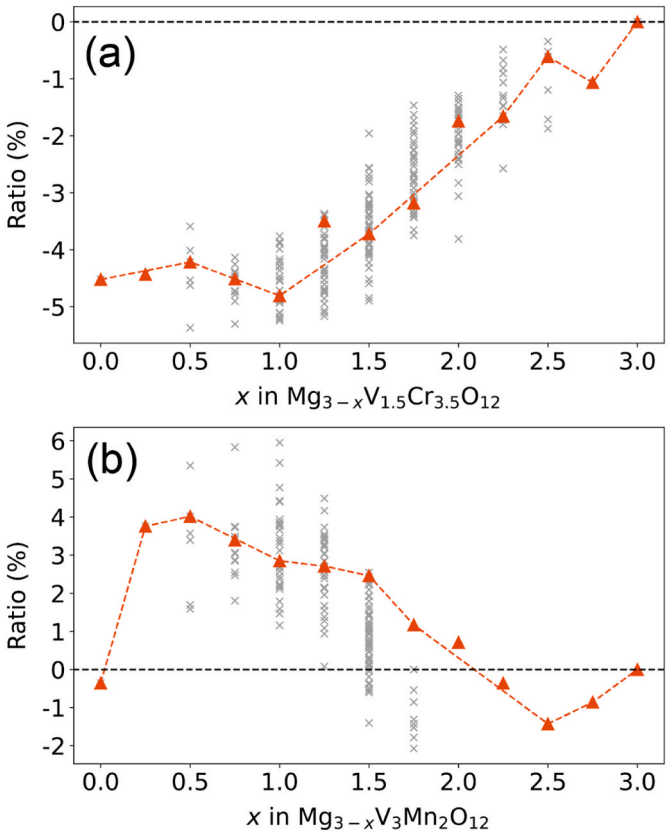

Fig. 7. Relative volume changes compared to the fully deintercalated structure for (a) $Mg_{3-x}V_{1.5}Cr_{3.5}O_{12}$ and (b) $Mg_{3-x}V_3Mn_2O_{12}$. Volume changes for symmetrically distinct structures are indicated by gray crosses, while those of energetically stable structures are shown in solid triangles. Intermediate metastable phases are connected via orange dashed lines.

To assess the chemical stability under operating conditions, AIMD simulations were performed at 300 K for 10 ps following an initial 10 ps equilibration period. As is shown in Fig. S2, the system exhibited stable total energy throughout the simulation, with no significant fluctuations, indicating strong structural and thermal stability at room temperature. Notably, both MVMO and MVCO retained their structural integrities without evidence of structural phase transition or bond dissociation, supporting their potential for practical applications in ambient battery environment.

3.4. Structural stability

Since the lifespan of cathode active materials is strongly influenced by structural stability, the structural stability of the candidate materials is assessed from the volume changes occurring during the full Mg-ion (de)intercalation process. Two graphs in Fig. 7 present the volume changes during the full intercalation process for the two garnet-type compounds. As is shown in Fig. 7(a), the volume of $Mg_{3-x}V_{1.5}Cr_{3.5}O_{12}$ slightly decreases from 4.5 % to 4.8 % maximum at $x = 1$ and steadily increases as x increases from 1 to 3, indicating a gradual expansion of the crystal structure compared to the fully intercalated state. In contrast, $Mg_{3-x}V_3Mn_2O_{12}$ reveals a more complex volume change behavior (Fig. 7 (b)). Initially, there is a significant increase in volume by 4 %, which is followed by a decrease to around −1.5 % at $x = 2.5$, and a slight increase thereafter. These results suggest that $Mg_3V_{1.5}Cr_{3.5}O_{12}$ undergoes a uniform expansion during intercalation by 3.0 % on average during the overall intercalation process, whereas $Mg_3V_3Mn_2O_{12}$ experiences comparable volumetric fluctuations with an average volume decrease of 1.9 %. This level of structural change is well within the acceptable range for

Table 1
Calculated elastic constants, bulk (B), shear (G) and Young's moduli (E) for $Mg_3V_{1.5}Cr_{3.5}O_{12}$ and $Mg_3V_3Mn_2O_{12}$ in charged and discharged states. B, G and E of $LiFePO_4$ [54] and $LiCoO_2$ [55] are presented for comparison purposes. All values are in units of GPa.

	C_{11}	C_{12}	C_{44}	B	G	E
$Mg_3V_{1.5}Cr_{3.5}O_{12}$	293.04	108.09	93.54	169.74	93.11	236.15
$V_{1.5}Cr_{3.5}O_{12}$	247.87	90.65	83.05	143.06	81.24	204.94
$Mg_3V_3Mn_2O_{12}$	188.43	150.76	97.37	163.32	51.23	139.13
$V_3Mn_2O_{12}$	252.47	96.82	91.67	148.70	85.86	216.00
$LiFePO_4$				93.9	48.4	123.9
$FePO_4$				73.6	51.4	125.0
$LiCoO_2$				171.95	111.38	165.74
CoO_2				96.87	41.71	108.52

rechargeable intercalation cathodes and favorably compares with both previously reported multivalent ion battery materials [47] and commercial lithium cathodes such as layered $LiCoO_2$ and olivine $LiFePO_4$ which have volume changes of 5.6 % and 6.8 %, respectively [48,49].

To further investigate structural changes, the variations in lattice parameters for both materials are presented in Fig. S3. These parameters include the lattice constants a, b, and c as well as the angles α, β, and γ between cell edges. As is shown in Fig. S3 (a-c) and (g-i), the lattice lengths exhibit tendency consistent with their volume changes with maximum deviation of approximately 4 % along the electrochemically stable path. In $Mg_{3-x}V_{1.5}Cr_{3.5}O_{12}$, the lattice length variation remains below 4 % for both chemically stable and unstable phases. In contrast, $Mg_{3-x}V_3Mn_2O_{12}$ exhibits similarly small changes in stable phases but exceeds 4 % in certain unstable configurations. The lattice angles remain nearly constant, except for the γ angle in $Mg_{3-x}V_3Mn_2O_{12}$, which deviates by approximately 4 % at $x = 1.5$. Overall, the modest changes in both lattice dimensions and volume suggest that mechanical

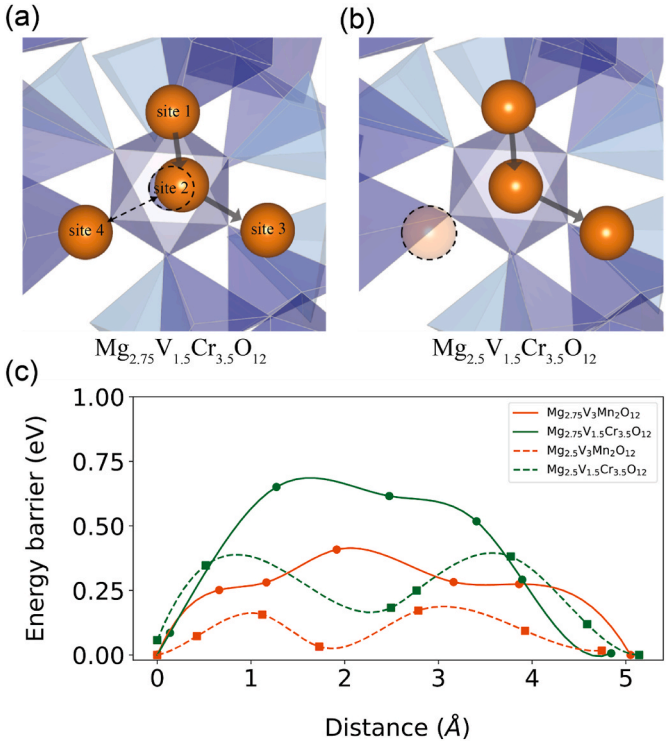

Fig. 8. Mg-ion migration path of (a) $Mg_{2.75}V_{1.5}Cr_{3.5}O_{12}$ and (b) $Mg_{2.5}V_{1.5}Cr_{3.5}O_{12}$. Site 1, 3 and 4 correspond to the centers of dodecahedra and site 2 corresponds to the center of octahedra. (c) Mg-ion migration barriers with five intermediate images are depicted in green solid line for $Mg_{2.75}V_{1.5}Cr_{3.5}O_{12}$, green dashed line for $Mg_{2.5}V_{1.5}Cr_{3.5}O_{12}$, red solid line for $Mg_{2.75}V_3Mn_2O_{12}$, and red dashed line for $Mg_{2.5}V_3Mn_2O_{12}$.

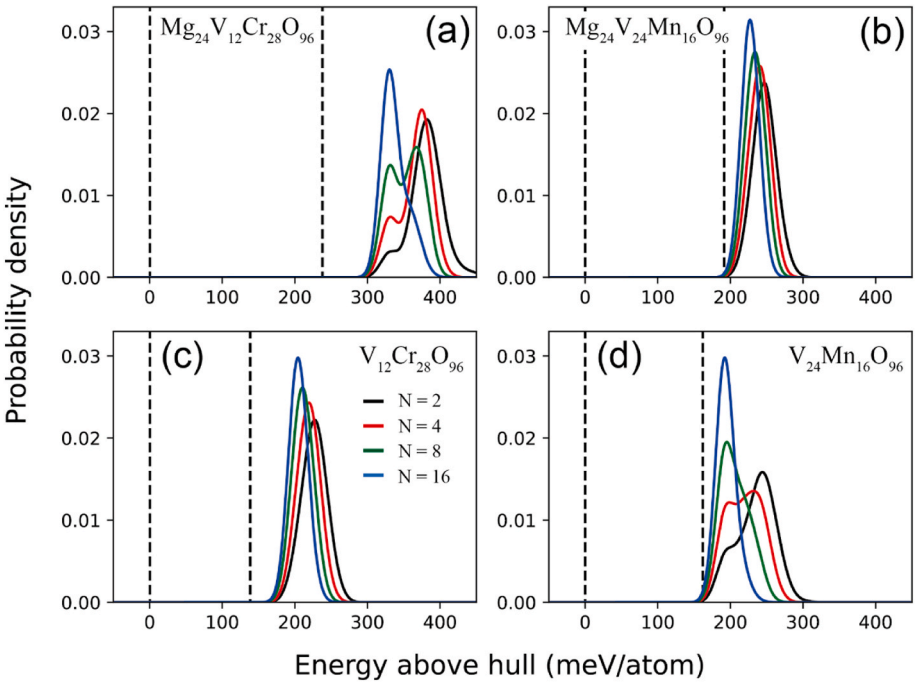

Fig. 9. E_{hull} for (a) $Mg_{24}V_{12}Cr_{28}O_{96}$, (b) $Mg_{24}V_{24}Mn_{16}O_{96}$, (c) $V_{12}Cr_{28}O_{96}$, and (d) $V_{24}Mn_{16}O_{96}$ with the corresponding PDFs for amorphous limits. In each plot, the left (right) dashed line represents the ground state energy (E_{hull}) of each material.

deformation during discharge is likely to be minimal.

Structural stability is also investigated from a mechanical viewpoint. It is known [50] that in terms of the elastic constants C_{ij}, the conditions for the mechanical stability of cubic structures are given by

$$C_{11} - |C_{12}| > 0, C_{11} + 2C_{12} > 0, C_{44} > 0.$$

As is seen from Table 1, the elastic constants for (de)intercalated phases of both $Mg_3V_{1.5}Cr_{3.5}O_{12}$ and $Mg_3V_3Mn_2O_{12}$ clearly satisfy the stability conditions. It is further noted that bulk (B), shear (G) and Young's moduli (E), which quantify resistance to volumetric and shape deformations, hold a special importance in battery applications since cathode materials are subjected to repeated volumetric changes during the (de)intercalation processes. Table 1 also shows a comparison of B, G and E between the proposed cathode materials and widely used Li-based cathode materials, $LiFePO_4$ and $LiCoO_2$. As is seen from the table, the elastic moduli of $Mg_3V_{1.5}Cr_{3.5}O_{12}$ and $Mg_3V_3Mn_2O_{12}$ are within the range of those of $LiFePO_4$ and $LiCoO_2$, which implies mechanical reliability during operation.

3.5. Mg-ion migration barrier

To investigate the Mg-ion diffusion within the host material, we employ the CI-NEB approach [35] to calculate the energy barrier for the Mg-ion migration, referred to as the migration barrier, which crucially affects the ion conductivity. For the garnet-type cathode materials, each Mg atom is neighbored by four magnesium atoms that are 3.73 Å (3.75 Å) apart for $Mg_3V_{1.5}Cr_{3.5}O_{12}$ ($Mg_3V_3Mn_2O_{12}$). It is found that the diffusion of Mg-ions follows a migration path from one dodecahedron center (site 1) to an adjacent dodecahedron center (site 3), mediated by an intermediate octahedron center (site 2) as illustrated in Fig. 8(a). The corresponding energy barrier is presented in Fig. 8(c) as a function of the migration distance for different compositions of the proposed cathode materials. For more discharged states, $Mg_{2.75}V_{1.5}Cr_{3.5}O_{12}$ and $Mg_{2.75}V_3Mn_2O_{12}$, the migration barriers are 687 meV and 415 meV, respectively. It is noted that the upper limits of the ion migration barrier are 525 meV for micron-sized particles and 650 meV for nano-sized particles, respectively, to ensure adequate battery operation [51]. The high migration barrier observed in $Mg_{2.75}V_{1.5}Cr_{3.5}O_{12}$ is attributed to the repulsion between the Mg ion at site 4 and the migrating Mg ion passing through site 2. This interaction results in an unstable migration path that deviates slightly from site 2, causing a less direct and more erratic trajectory (Fig. 8(a)).

To address this issue, additional magnesium vacancy is introduced by removing the Mg ion at site 4 in Fig. 8(a). This adjustment allows the Mg ion passing through site 2 to follow a more stable migration path, as depicted in Fig. 8(b), which results in the reduction of the migration barrier to 395 meV for $Mg_{2.5}V_{1.5}Cr_{3.5}O_{12}$ and 190 meV for $Mg_{2.5}V_3Mn_2O_{12}$, respectively. These reduced migration barriers are comparable to those reported for other multivalent ion battery materials [47] and fall within commercially viable ranges, suggesting that even with minimal Mg-ion extraction, the proposed cathode materials can achieve efficient ion conductivity, which proves their high potential for practical applications in Mg-ion batteries.

3.6. Synthesizability

While evaluating battery performance is an important task for the newly proposed cathode active materials, it is also of great interest to assess their thermodynamic stability to determine if the materials can be synthesized and maintained under practical conditions. To this end, the energy above hull (E_{hull}) calculations, which states the relative stability of a compound with respect to the most stable phases of the same composition, are employed. In cases of $Mg_3V_{1.5}Cr_{3.5}O_{12}$ and $Mg_3V_3Mn_2O_{12}$, the energies above the hull are 237.7 and 191.3 meV per atom, respectively, and for their deintercalated phases, $V_{1.5}Cr_{3.5}O_{12}$ and $V_3Mn_2O_{12}$, the energies above hull are 138.8 and 162 meV per atom, respectively. An energy above hull less than approximately 50 meV per atom is generally considered to indicate a high likelihood of stability and synthesizability under typical conditions. It should be noted, however, that according to the Materials Projects database [33], 40.5 % of oxides with $E_{hull} \leq 50$ meV/atom have been experimentally confirmed, and moreover, 25.2 % of oxides with $50 \leq E_{hull} \leq 250$ meV per atom have been experimentally verified. This observation suggests that while a lower energy above hull generally implies a higher likelihood of

Table 2
Voltage (V), theoretical capacity (mAh/g), migration barrier (meV), and volume change (%) for $Mg_3V_{1.5}Cr_{3.5}O_{12}$, $Mg_3V_3Mn_2O_{12}$, $LiCoO_2$, and $LiFePO_4$ are listed for comparison.

	Voltage (V)	Capacity (mAh/g)	Migration barrier (meV)	Volume change (%)
MVCO	2.78	306.8	395	4.8
MVMO	2.69	304.8	190	4
$LiCoO_2$	3.75	294	210–310	5.6
$LiFePO_4$	3.47	170	190	6.8

synthesizability, a significant number of materials within 50–250 meV/atom range of E_{hull} are also experimentally realizable. For instance, garnet-structured compounds such as $Gd_3Sc_2(GaO_4)_3$, $Ba_3Al_2(SiO_4)_3$ and $Mg_3Mn_2(SiO_4)_3$ have been experimentally synthesized despite exhibiting relatively high E_{hull} of around 691, 272 and 115 meV per atom, respectively, further supporting the notion that metastable garnet structures can still be synthesizable [52,53].

To gain further insights into synthesizability, the energies of the corresponding amorphous structures are calculated since they represent the thermodynamic upper limits to the free energy scale for synthesizability of metastable crystalline polymorphs [37]. As is seen from the PDFs presented in Fig. 9(a) and (c), the proposed materials have their energies above the hull predominantly below the corresponding amorphous limits, demonstrating a high likelihood of successful synthesis of $Mg_3V_{1.5}Cr_{3.5}O_{12}$ and $V_{1.5}Cr_{3.5}O_{12}$. In contrast, the PDFs presented in Fig. 9(b) and (d) reveal that the deintercalated structures exhibit E_{hull} close to the lower bound on their respective amorphous limits. However, the portions of the area under the PDFs lower than E_{hull} for $Mg_3V_3Mn_2O_{12}$ and $V_3Mn_2O_{12}$ are merely 6×10^{-3} and 5×10^{-4}, respectively, with a sample size of $N = 16$, which suggests that the deintercalated states also have a sufficient likelihood of successful synthesis.

4. Conclusion

In the present study, we have proposed two promising candidates for Mg-ion cathode active materials: $Mg_3V_{1.5}Cr_{3.5}O_{12}$ and $Mg_3V_3Mn_2O_{12}$. DFT calculations have revealed that these materials exhibit high voltages of 2.79V and 2.69V and outstanding energy densities of 856 Wh/kg and 821 Wh/kg, respectively. Additionally, Mg-ions in these materials are shown to have low energy barriers for migration which will be beneficial during the (de)intercalation process. Furthermore, the calculations of the corresponding amorphous limits indicate that both materials are highly likely to be synthesized. Table 2 presents the voltages, theoretical capacities, migration barrier and volume changes of $Mg_3V_{1.5}Cr_{3.5}O_{12}$ and $Mg_3V_3Mn_2O_{12}$ together with those of commercial Li-ion cathode, $LiCoO_2$ and $LiFePO_4$. This comparison certainly demonstrates the potential of $Mg_3V_{1.5}Cr_{3.5}O_{12}$ and $Mg_3V_3Mn_2O_{12}$ as high-performance cathode active materials that can be as competitive as Li-based cathode materials. The development of the new cathode materials can drive advancement in battery industry, which could contribute to the broader adoption of Mg-ion batteries in various technological sectors, including electric vehicles and grid-scale energy storage applications.

CRediT authorship contribution statement

Sanghyun Kim: Writing – review & editing, Writing – original draft, Investigation, Formal analysis, Data curation, Conceptualization. **Joo-Hyoung Lee:** Writing – review & editing, Supervision, Project administration, Funding acquisition, Formal analysis, Conceptualization.

Declaration of competing interest

The authors declare that they have no known competing financial interests or personal relationships that could have appeared to influence the work reported in this paper.

Acknowledgements

This work was supported by the GIST-MIT Collaboration grant funded by GIST in 2025 and the National Research Foundation of Korea grant funded by the Korea Government (MSIT) (RS-2023-NR119931).

Appendix A. Supplementary data

Supplementary data to this article can be found online at https://doi.org/10.1016/j.mtadv.2025.100603.

Data availability

Data will be made available on request.

References

[1] J.M. Tarascon, M. Armand, Issues and challenges facing rechargeable lithium batteries, Nature 414 (2001) 359–367.
[2] J.B. Goodenough, K.S. Park, The Li-ion rechargeable battery: a perspective, J. Am. Chem. Soc. 135 (2013) 1167–1176.
[3] M. Armand, J.-M. Tarascon, Building better batteries, Nature 451 (2008) 652–657.
[4] D. Larcher, J.M. Tarascon, Towards greener and more sustainable batteries for electrical energy storage, Nat. Chem. 7 (2015) 19–29.
[5] M. Arbabzadeh, J.X. Johnson, G.A. Keoleian, P.G. Rasmussen, L.T. Thompson, Twelve principles for green energy storage in grid applications, Environ. Sci. Technol. 50 (2016) 1046–1055.
[6] B.V. Ratnakumar, M.C. Smart, A. Kindler, H. Frank, R. Ewell, S. Surampudi, Lithium batteries for aerospace applications: 2003 Mars Exploration Rover, J. Power Sources 119–121 (2003) 906–910.
[7] W. Liu, P. Oh, X. Liu, M.J. Lee, W. Cho, S. Chae, Y. Kim, J. Cho, Nickel-rich layered lithium transition-metal oxide for high-energy lithium-ion batteries, Angew. Chem. Int. Ed. 54 (2015) 4440–4457.
[8] A. Manthiram, J.C. Knight, S.T. Myung, S.M. Oh, Y.K. Sun, Nickel-rich and lithium-rich layered oxide cathodes: progress and perspectives, Adv. Energy Mater. 6 (2016) 1501010.
[9] M.M. Huie, D.C. Bock, E.S. Takeuchi, A.C. Marschilok, K.J. Takeuchi, Cathode materials for magnesium and magnesium-ion based batteries, Coord. Chem. Rev. 287 (2015) 15–27.
[10] H.D. Yoo, I. Shterenberg, Y. Gofer, G. Gershinsky, N. Pour, D. Aurbach, Mg rechargeable batteries: an on-going challenge, Energy Environ. Sci. 6 (2013) 2265–2279.
[11] C. Zhang, Z.H. Wu, C.Q. Yang, X.Z. Guo, Y.X. Yu, Y. Yang, Rational regulation of optimal oxygen vacancy concentrations on VO_2 for superior aqueous zinc-ion battery cathodes, ACS Appl. Mater. Interfaces 16 (2024) 40903–40913.
[12] Z.H. Wu, Y.X. Yu, A.N. Chibisov, Density functional theory investigation on fast storage of sodium and potassium in Ni_2TeO_6 as a novel promising cathode material, Mater. Today Energy 37 (2023).
[13] X. Feng, M. Ouyang, X. Liu, L. Lu, Y. Xia, X. He, Thermal runaway mechanism of lithium ion battery for electric vehicles: a review, Energy Storage Mater. 10 (2018) 246–267.
[14] H. Liu, Z. Wei, W. He, J. Zhao, Thermal issues about Li-ion batteries and recent progress in battery thermal management systems: a review, Energy Convers. Manag. 150 (2017) 304–330.
[15] M. Matsui, Study on electrochemically deposited Mg metal, J. Power Sources 196 (2011) 7048–7055.
[16] A.J. Crowe, J.L. Dimeglio, K.K. Stringham, B.M. Bartlett, Kinetics of Magnesium deposition and stripping from non-aqueous electrolytes, J. Phys. Chem. C 121 (2017) 20613–20620.
[17] O. Tutusaus, R. Mohtadi, T.S. Arthur, F. Mizuno, E.G. Nelson, Y.V. Sevryugina, An efficient halogen-free electrolyte for use in rechargeable magnesium batteries, Angew. Chem. Int. Ed. 54 (2015) 7900–7904.
[18] C. Ling, D. Banerjee, W. Song, M. Zhang, M. Matsui, First-principles study of the magnesiation of olivines: redox reaction mechanism, electrochemical and thermodynamic properties, J. Mater. Chem. 22 (2012) 13517–13523.
[19] Z.L. Tao, L.N. Xu, X.L. Gou, J. Chen, H.T. Yuan, TiS_2 nanotubes as the cathode materials of Mg-ion batteries, Chem. Commun. (2004) 2080–2081.
[20] M. Liu, Z. Rong, R. Malik, P. Canepa, A. Jain, G. Ceder, K.A. Persson, Spinel compounds as multivalent battery cathodes: a systematic evaluation based on ab initio calculations, Energy Environ. Sci. 8 (2015) 964–974.
[21] H. Liu, Y. Cai, Z. Guo, J. Zhou, Two-dimensional V_2N MXene monolayer as a high-capacity anode material for lithium-ion batteries and beyond: first-principles calculations, ACS Omega 7 (2022) 17756–17764.

[22] E. Levi, A. Mitelman, D. Aurbach, M. Brunelli, Structural mechanism of the phase transitions in the Mg-Cu-Mo_6S_8 system probed by ex situ synchrotron X-ray diffraction, Chem. Mater. 19 (2007) 5131–5142.
[23] T. Xie, J.C. Grossman, Crystal graph convolutional neural networks for an accurate and interpretable prediction of material properties, Phys. Rev. Lett. 120 (2018) 145301.
[24] E.G. Ahn, J.H. Yang, J.H. Lee, $Mg_3Si_3(MoO_6)_2$ as a high-performance cathode active material for magnesium-ion batteries, ACS Appl. Mater. Interfaces 13 (2021) 47749–47755.
[25] M. Andrut, M. Wildner, The crystal chemistry of birefringent natural uvarovites. Part III. Application of the superposition model of crystal fields with a characterization of synthetic cubic uvarovite, Phys. Chem. Miner. 29 (2002) 595–608.
[26] C. Liu, Z. Xia, M.S. Molokeev, Q. Liu, Synthesis, crystal structure, and enhanced luminescence of garnet-type $Ca_3Ga_2Ge_3O_{12}$:Cr^{3+} by codoping Bi^{3+}, J. Am. Ceram. Soc. 98 (2015) 1870–1876.
[27] G. Kresse, J. Furthmuller, Efficient iterative schemes for ab initio total-energy calculations using a plane-wave basis set, Phys. Rev. B 54 (1996) 11169–11186.
[28] P.E. Blöchl, Projector augmented-wave method, Phys. Rev. B 50 (1994) 17953–17979.
[29] J.P. Perdew, K. Burke, M. Ernzerhof, Generalized gradient approximation made simple, Phys. Rev. Lett. 77 (1996) 3865–3868.
[30] J.D. Pack, H.J. Monkhorst, Special points for Brillouin-zone integrations, Phys. Rev. B 13 (1976) 5188–5192.
[31] A. Jain, G. Hautier, S.P. Ong, C.J. Moore, C.C. Fischer, K.A. Persson, G. Ceder, Formation enthalpies by mixing GGA and GGA + U calculations, Phys. Rev. B 84 (2011) 1–10.
[32] L. Wang, T. Maxisch, G. Ceder, Oxidation energies of transition metal oxides within the GGA+U framework, Phys. Rev. B 73 (2006) 1–6.
[33] A. Jain, S.P. Ong, G. Hautier, W. Chen, W.D. Richards, S. Dacek, S. Cholia, D. Gunter, D. Skinner, G. Ceder, K.A. Persson, Commentary: the materials project: a materials genome approach to accelerating materials innovation, APL Mater. 1 (2013) 011002.
[34] Y.X. Yu, Theoretical insights into surface-phase transition and ion competition during alkali ion intercalation on the Cu_4Se_4 nanosheet, Phys. Chem. Chem. Phys. 26 (2024) 323–335.
[35] Graeme Henkelman, B.P. Uberuaga, H. Jonsson, A climbing image nudged elastic band method for finding saddle points and minimum energy paths, J. Chem. Phys. 113 (2000) 9901–9904.
[36] R. Nelson, C. Ertural, J. George, V.L. Deringer, G. Hautier, R. Dronskowski, LOBSTER: local orbital projections, atomic charges, and chemical-bonding analysis from projector-augmented-wave-based density-functional theory, J. Comput. Chem. 41 (2020) 1931–1940.
[37] M. Aykol, S.S. Dwaraknath, W. Sun, K.A. Persson, Thermodynamic limit for synthesis of metastable inorganic materials, Sci. Adv. 4 (2018) 1–7.
[38] S.P. Ong, W.D. Richards, A. Jain, G. Hautier, M. Kocher, S. Cholia, D. Gunter, V. L. Chevrier, K.A. Persson, G. Ceder, Python materials genomics (pymatgen): a robust, open-source python library for materials analysis, Comput. Mater. Sci. 68 (2013) 314–319.
[39] Y.-X. Yu, Sodium/Potassium intercalation on the Cu_4S_4 nanosheet accompanied by a surface phase transition and their competition with protons, ACS Appl. Energy Mater. 6 (2023) 10048–10060.
[40] A. Urban, D.H. Seo, G. Ceder, Computational understanding of Li-ion batteries, npj Comput. Mater. 2 (2016) 16002.
[41] X.B. Jia, J. Wang, Y.F. Liu, Y.F. Zhu, J.Y. Li, Y.J. Li, S.L. Chou, Y. Xiao, Facilitating layered oxide cathodes based on orbital hybridization for sodium-ion batteries: marvelous air stability, controllable high voltage, and anion redox chemistry, Adv. Mater. 36 (2024) 1–31.
[42] R. Fukuma, M. Harada, W. Zhao, M. Sawamura, Y. Noda, M. Nakayama, M. Goto, D. Kan, Y. Shimakawa, M. Yonemura, N. Ikeda, R. Watanuki, H.L. Andersen, A. M. D'Angelo, N. Sharma, J. Park, H.R. Byon, S. Fukuyama, Z. Han, H. Fukumitsu, M. Schulz-Dobrick, K. Yamanaka, H. Yamagishi, T. Ohta, N. Yabuuchi, Unexpectedly large contribution of oxygen to charge compensation triggered by structural disordering: detailed experimental and theoretical study on a Li_3NbO_4−NiO binary system, ACS Cent. Sci. 8 (2022) 775–794.
[43] H. Yao, Air-stability of sodium-based layered-oxide cathode materials, Sci. China Chem. 65 (2022) 1076–1087.
[44] N. Voronina, S.T. Myung, Recent advances in electrode materials with anion redox chemistry for sodium-ion batteries, Energy Mater. Adv. 2021 (2021) 9819521.
[45] X. Cao, Y. Qiao, M. Jia, P. He, H. Zhou, Ion-exchange: a promising strategy to design Li-Rich and Li-Excess layered cathode materials for Li-Ion batteries, Adv. Energy Mater. 12 (2022) 1–14.
[46] B. Mortemard De Boisse, G. Liu, J. Ma, S.I. Nishimura, S.C. Chung, H. Kiuchi, Y. Harada, J. Kikkawa, Y. Kobayashi, M. Okubo, A. Yamada, Intermediate honeycomb ordering to trigger oxygen redox chemistry in layered battery electrode, Nat. Commun. 7 (2016) 1–9.
[47] Y.X. Yu, High storage capacity and small volume change of potassium-intercalation into novel vanadium oxychalcogenide monolayers V_2S_2O, V_2Se_2O and V_2Te_2O: an ab initio DFT investigation, Appl. Surf. Sci. 546 (2021) 149062.
[48] X. Wang, R. Xiao, H. Li, L. Chen, Quantitative structure-property relationship study of cathode volume changes in lithium ion batteries using ab-initio and partial least squares analysis, J. Materiomics 3 (2017) 178–183.
[49] T.V.S.L. Satyavani, A. Srinivas Kumar, P.S.V. Subba Rao, Methods of synthesis and performance improvement of Lithium iron phosphate for high rate Li-ion batteries: a review, Eng. Sci. Technol. Int. J. 19 (2016) 178–188.
[50] Z.J. Wu, E.J. Zhao, H.P. Xiang, X.F. Hao, X.J. Liu, J. Meng, Crystal structures and elastic properties of superhard IrN_2 and IrN_3 from first principles, Phys. Rev. B 76 (2007) 1–15.
[51] Z. Rong, R. Malik, P. Canepa, G. Sai Gautam, M. Liu, A. Jain, K. Persson, G. Ceder, Materials design rules for multivalent ion mobility in intercalation structures, Chem. Mater. 27 (2015) 6016–6021.
[52] G.A. Novarl atto G V Grnns, The crystal chemistry of the silicate garnets, Am. Mineral. 56 (1971) 791–825.
[53] H. Hua, S. Mirov, Y.K. Vohra, High-pressure and high-temperature studies on oxide garnets, Phys. Rev. B 54 (1996) 6200–6209.
[54] T. Maxisch, G. Ceder, Elastic properties of olivine Li_xFePO_4 from first principles, Phys. Rev. B 73 (2006) 1–4.
[55] L. Wu, J. Zhang, Ab initio study of anisotropic mechanical properties of $LiCoO_2$ during lithium intercalation and deintercalation process, J. Appl. Phys. 118 (2015) 225101.